

## MODELLING AND SIMULATION FOR INNOVATIVE AERONAUTIC DEVELOPMENTS

W.J. Vankan<sup>1</sup>, N. van Hoorn<sup>1</sup>, A.J. de Wit<sup>1</sup>, and R. Maas<sup>1</sup>

<sup>1</sup> Royal Netherlands Aerospace Centre NLR, Aerospace Vehicles Division, Collaborative Engineering Systems Department, Anthony Fokkerweg 2, 1059 CM Amsterdam, The Netherlands  
e-mail: [jos.vankan@nlr.nl](mailto:jos.vankan@nlr.nl)

---

### Abstract

*Radical innovations are necessary to achieve the long-term goals of global aviation on greenhouse gas reductions. Many innovative technologies are already being investigated. The correct implementation of these innovative technologies is only possible if accurate prediction of their implications can be made. For that purpose, advanced modelling, simulation and optimization methodologies are indispensable. Three different examples of these methodologies will be presented in this paper, including some illustrative applications. One example deals with the use of advanced 3D finite element method (FEM) modelling for prediction of relevant electro-magnetic (EM) phenomena like induction. Such EM simulation supports induction welding (IW) processes which can be used in the innovative assembly of thermo-plastic (TP) carbon fiber reinforced polymer (CFRP) composite components. A second example looks at the optimized 3D placement of electric components in dedicated compartments on hybrid-electric propulsion aircraft concepts. Fundamental methodologies for computational geometry and graph-based routing modelling can be used to efficiently address such problems. A third example looks at the design and optimization of advanced flaps on large passenger aircraft. Different disciplines like structural design, manufacturing- and cost modelling and performance prediction are needed in such optimizations. The relatively complex multi-disciplinary model that results from this, can be efficiently evaluated, assessed and optimized using surrogate-based optimization approaches. The 3 examples illustrate how novel aircraft technologies are supported by increasingly digitalized methods, tools and models.*

**Keywords:** induction welding, TP-CFRP, space allocation, components placement, routing optimization, Multidisciplinary Design Optimization.

---

## 1 INTRODUCTION

Radical innovations are necessary to achieve the long-term goals of global aviation on green-house gas reductions. Many innovative technologies are already being investigated, for example technologies related to advanced composite airframe structures developments, more electric systems for propulsion and advanced flight controls. These innovative technologies are found in different application areas of the aircraft development process. New materials and structures technologies, for instance, are aiming for lighter airframe structures with better properties for manufacturability and environmental footprint. For example, thermo-plastic (TP) carbon fiber reinforced polymer (CFRP) composites are being investigated for their improved light-weight potential, their faster production and assembly processes, and their possibilities for recycling [1]. New technologies for more electric or hybrid-electric propulsion (HEP) systems are aiming at direct reduction of fuel consumption of the aircraft power plant [2]. This implies the use of much more electric components on board aircraft for the propulsion power train and control systems [3]. New technologies for more advanced flight controls are aimed at improved primary flight control surfaces for lower weight, lower cost and better performance. For example, advanced flaps are designed to take these different aspects into account simultaneously [4].

The correct application of all these innovative technologies is only possible if accurate prediction of their implications can be made. For that purpose, advanced modelling, simulation and optimization methodologies are indispensable. For example, in the assembly of TP CFRP composite components, innovative joining methods like induction welding (IW) can be used. However, the exact behavior of the material in such electro-magnetic (EM) heating processes is very intricate and difficult to predict. The three-dimensional (3D) nature of the phenomena taking place requires a detailed analysis of the process. The use of advanced 3D finite element method (FEM) modelling allows for such detailed analysis and helps to predict the relevant EM phenomena. For the investigation of increased numbers and higher power electric components on board aircraft, one of the challenges is the detailed placement of these components in dedicated compartments. The optimization of the volumetric space allocation of these components is a typical target, taking into account constraints on inter-component clearance or on thermal limitations. Another typical target is the optimization of inter-connectivity of cables between components aiming for minimal length and mass, and accounting for certain routing constraints. Fundamental methodologies for computational geometry and graph-based routing modelling can be used to efficiently address such problems. For the design and optimization of advanced flaps, some representation of the different disciplines of structural design, manufacturing- and cost modelling and performance prediction are needed. The relatively complex multi-disciplinary model that results from this, may be efficiently evaluated, assessed and optimized using surrogate-based optimization approaches. In that way the overall flap assessment can be done in very limited time and directions and limitations for the flap design can be estimated.

These example applications represent some cases in which the development of innovative technologies for novel aircraft is supported by increasingly digitalized methods, tools and technologies. In this paper these example applications will be elaborated on and their potential implications on innovative aeronautic technologies will be indicated. The investigations behind these example applications have been executed in the Clean Sky 2 project STUNNING and in the Horizon 2020 project AGILE 4.0 [5].

## 2 ELECTRO-MAGNETIC FEM MODELLING FOR INDUCTION WELDING

In the assembly of light-weight aircraft structures, TP CFRP composite laminates are increasingly utilized. These TP composites can be locally re-melted, allowing them to be joined via welding. An example of an innovative joining technique is welding by local electromagnetic inductive heating, so-called induction welding. Several heating mechanisms take place in the inductive heating of TP CFRP. The extent in which each mechanism contributes to the heating process, depends on the composite material that is heated and the electromagnetic induction process parameters that are applied. At present, the inductive heating of woven fabric composites is well documented and understood [6]. However, the inductive heating of Uni-Directional (UD) ply CFRP material is much less understood. According to literature [7] this could be due to the absence of current returning paths that are required for the inductive eddy currents, which are responsible for the main heating mechanism.

In this paper we present a 3D electromagnetic simulation model that can predict the 3D energy source field from local Joule heating due to induced electric currents in the CFRP laminate. This electromagnetic model can be coupled to 3D thermal simulation models that can provide insight into the actual heating of TP CFRP laminate. Specific aspects that are addressed in these simulations include the influence of the UD plies and their orientations on the eddy current generation and on the heat generation inside the CFRP laminate that is placed in an electromagnetic field that is induced by an electric coil.

To investigate the exact behavior of the induced electric currents in the CFRP laminate, we consider a simplified experimental set-up. In this set-up we use a large, more or less rectangular water-cooled tubular copper coil with a straight leg just above the laminate, where it generates a relatively simple and well-defined electromagnetic field. The same simplified experimental set-up is defined in a FEM electromagnetic simulation model, which is implemented in the FEM software Simulia-Abaqus [8], see Figure 1. The FEM electromagnetic simulation model can have a double planar symmetry in the two vertical center-planes: one perpendicular to the coil and one through the center-line of the coil. This symmetry is the case if the cross-ply laminate has only 0- and/or 90-degree plies that are oriented parallel and perpendicular to the coil center-line. In that case only one quadrant of the domain needs to be considered in the simulation model; in all other cases the full domain shall be considered.

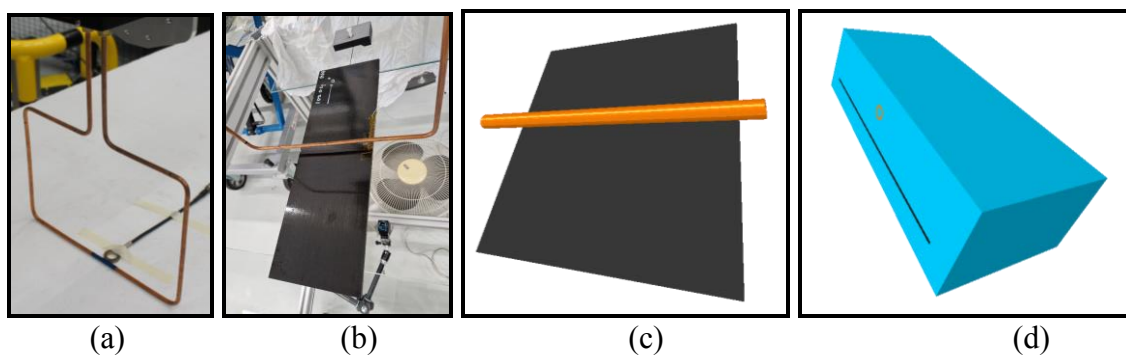


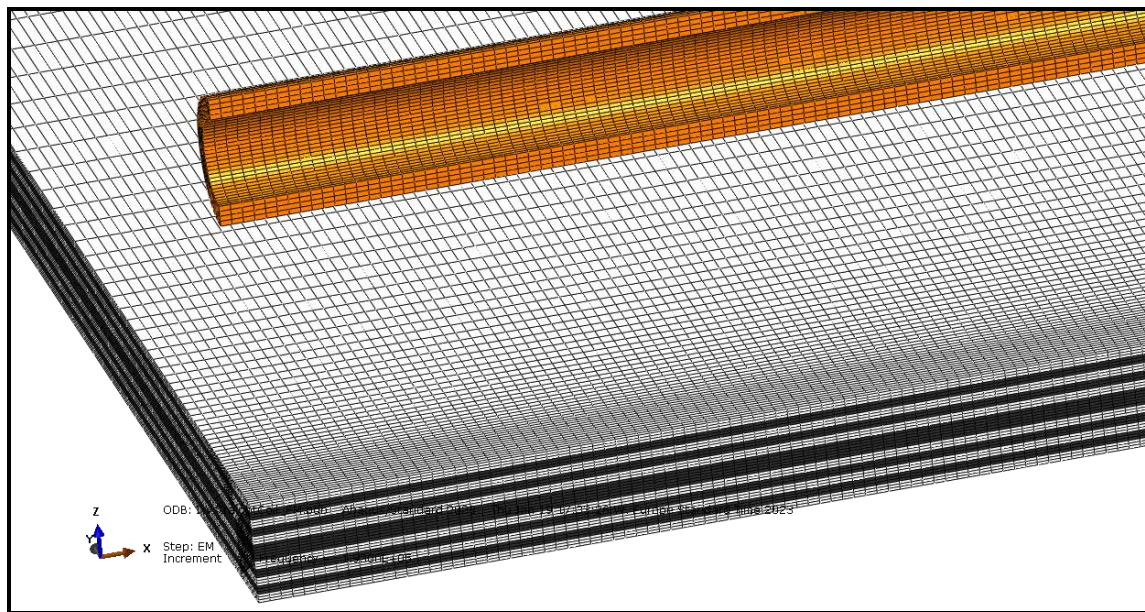
**Figure 1** Illustration of the simplified experimental set-up and its implementation in a FEM electromagnetic simulation model. From left to right, it is shown: (a): the more or less rectangular copper coil; (b): the straight leg of the coil just above the laminate (black plate); (c): the FEM simulation model of the straight leg of the coil (orange) and the laminate (black), which can have a double planar symmetry in the two vertical center-planes: one perpendicular to the coil and one through the center-line of the coil; (d) the right half of the considered simulation domain, where also the air is indicated in blue.

As indicated in the Figure 1, the FEM electromagnetic simulation model contains three different material sections: the copper coil, the composite laminate plies and the surrounding air [9]. The composite laminate contains consolidated UD plies of the pre-preg material Toray TC1320 PEKK AS4D [10]. For the coil standard copper CU-ETP1 – C11040 is assumed, and atmospheric air at sea level is assumed. The electromagnetic properties that must be prescribed for these materials are given in Table 1 [9].

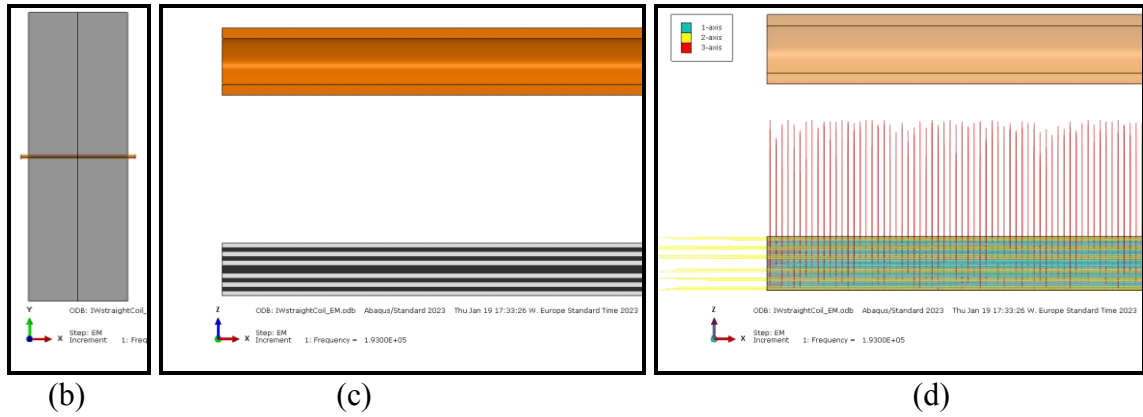
**Table 1** The electromagnetic properties that must be prescribed for the 3 different material sections in the FEM electromagnetic simulation model. For the coil, an electric conductivity of 1.0 S/m is used in the simulations to simplify the prescribed current density and avoid substantial self-inductance effects in the coil.

	Electric conductivity [S/m]	Magnetic permeability [H/m]	Dielectric constant (Electrical Permittivity) [F/m]
Air	1.0	1.26E-6	8.85E-12
Coil	1.0 (60.0E6)	1.26E-6	8.85E-12
Ply	fiber direction: 33500.0 cross-fiber direction: 1.0 thickness direction: 1.0	1.26E-6	8.85E-12

With the composite ply properties, the various plies and their thicknesses and orientations can be easily defined for any laminate in the FEM electromagnetic simulation model. A solid FEM mesh with HEX elements is used, where typically each ply is modelled by one or more layers of element in thickness direction. Typical TP CFRP ply thicknesses are in the order of 0.1mm and typical size of the 3D domain for the FEM electromagnetic simulation is in the order of 100mm in each direction. So, the FEM problem size for the fully discretized 3D domain can grow quite large if a laminate with many plies is considered. Here we consider a domain of approximately 120mm by 120mm in the laminate in-plane directions, and 40mm in the laminate out-of-plane direction. The total domain is discretized into 2372656 linear 8 node HEX elements of type EMC3D8 [8]. A symmetric [0,90]-cross-ply composite laminate layup is considered with ply thickness of 0.138mm and 36 plies with ply angles:  $[90_3, 0_3]_{3s}$ . See Figure 2.



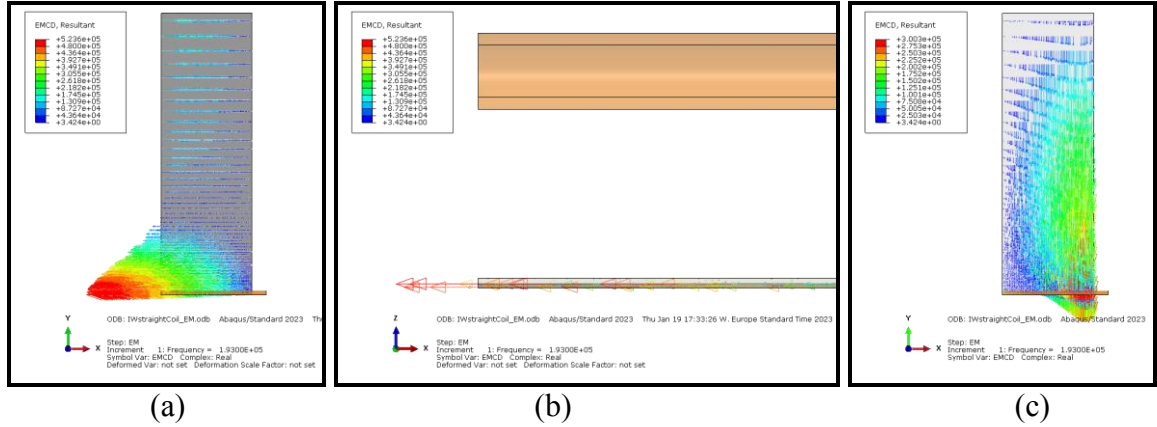
(a)



**Figure 2 Illustration of the FEM electromagnetic simulation model. (a): iso-view on the mesh of the considered 3D domain showing only the coil (orange) and laminate (black, white). (b): Top view in -Z direction of the considered double symmetric 3D domain showing only the coil (orange) and laminate (grey), in which the analyses are done only on the upper-right quadrant. (c): Front view in +Y direction on the vertical cross-section of the domain through the center line of the coil, where in the bottom the 0-degree plies are indicated in black and the 90-degree plies are indicated in white. (d): Front view in +Y direction on the vertical cross-section of the domain through the center line of the coil, where in the bottom the element orientation vectors of the plies in the laminate are shown.**

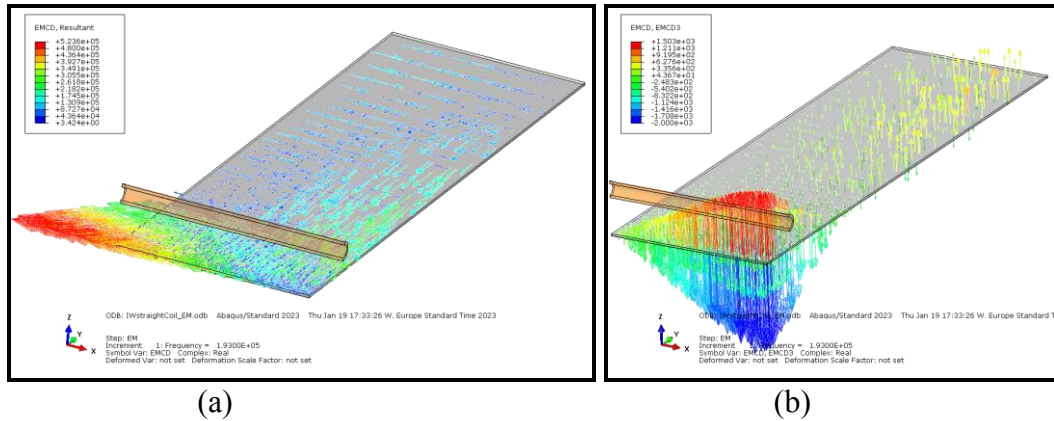
In the FEM electromagnetic simulation, a constant AC current with a frequency of 193kHz is prescribed in the coil as a current density of  $11.87\text{A/mm}^2$  in length direction of the coil. This directly corresponds to the 199.5A and 193kHz AC current that is applied to the coil in the experiment. The coil is placed at a distance of 14mm above the laminate, i.e. an air gap of 14mm exists between the coil and the upper surface of the laminate. The AC current in the coil creates an electromagnetic field in and around the coil, and induces eddy currents in the composite laminate. The local strength of these eddy currents is mainly determined by the local strength and orientations of the electromagnetic field and the local conductivity properties and orientations of the plies in the composite laminate. As indicated in Table 1, the ply conductivity is very high in fiber direction and very low perpendicular to the fibers, which is a result of the very high conductivity of the carbon fibers and very low conductivity of the TP matrix material. Due to these local orientations of the ply conductivities and of the electromagnetic field, very specific patterns of induced currents will appear in the plies. In the FEM electromagnetic simulation these induced currents are calculated as local electromagnetic current density (EMCD) vectors. In the composite laminate these EMCD vectors typically are aligned with the local fiber direction because that is where the highest conductivity exists. In the considered cross-ply laminate the fiber directions in the upper three 90-degree plies are perpendicular to the coil direction, in the three 0-degree plies below the fiber directions are aligned with the coil direction. According to Lenz' law the induced currents in the laminate are such that they counteract the change of magnetic field from the coil. Consequently, the highest induced currents occur in the 0-degree plies right below the coil, which is in global -X-direction in the domain, Figure 3.





**Figure 3** Illustration of the electromagnetic current densities (EMCD) in the laminate: (a): Top view on the EMCD vectors in the 0-degree plies nrs. 31-33: high EMCD in  $-X$ -direction is obvious below the coil, and increased EMCD in  $+X$ -direction near the far edge of the laminate in the top of the picture. (b) Front view in global  $+Y$ -direction on the cross-section of the coil (top) and the upper 6 plies nrs. 31-36 of the laminate (bottom), where it is shown that the high EMCD vectors occur only in the 0-degree plies nrs. 31-33, and EMCD in the 90-degree plies nrs. 34-36 is very low. (c): Top view on the EMCD vectors in the 90-degree plies 34-36: high EMCD in  $-Y$ -direction occurs along the right edge of the laminate. The vector plots show the complex-real part of EMCD solution.

Because in the 0-degree plies the conductivity in global  $Y$ -direction is very low, there are no high return-currents in these plies, i.e. currents that close a loop in the laminate from which a counteracting magnetic field originates. Instead, these high return-currents in  $+Y$ - and  $-Y$ -directions occur in the adjacent 90-degree plies where the conductivity in global  $Y$ -directions is very high, see Figure 4. In consequence, increased return-currents in global  $+X$ -direction occur again in the 0-degree plies near the edges of the laminate far away from the coil so in relatively low electromagnetic field strength. Furthermore, also inter-ply exchange currents occur as locally increased current density vector components in thickness direction of the laminate, i.e. in global  $Z$ -direction. These inter-ply exchange currents also contribute to the current-loop in the laminate from which the counteracting magnetic field originates.



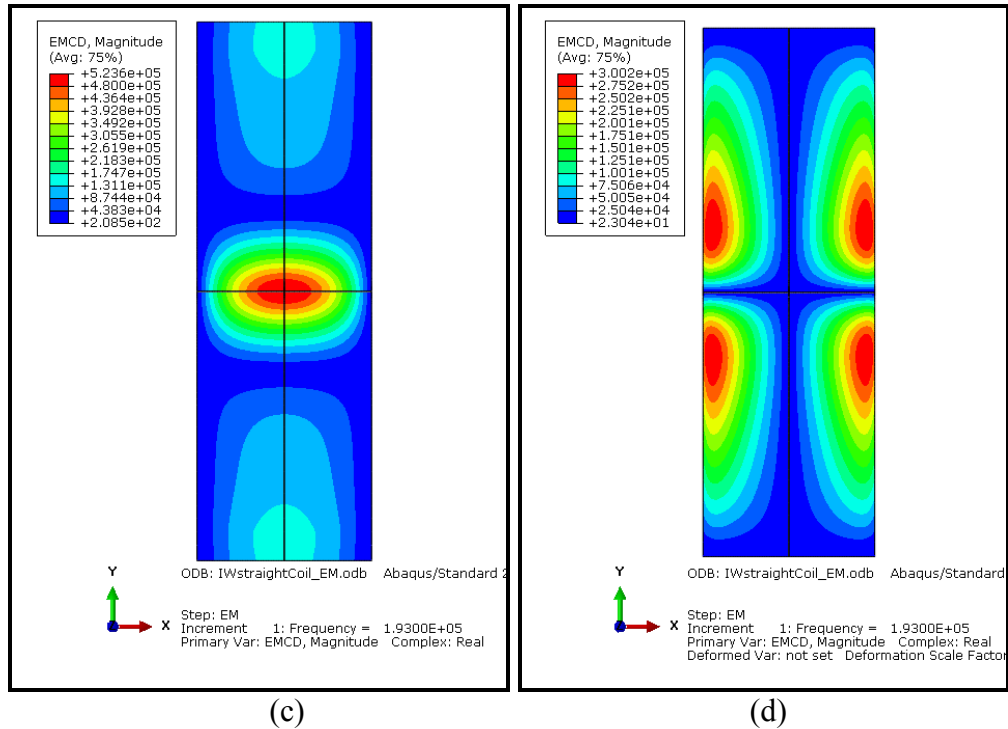


**Figure 4** Illustration of the electromagnetic current densities (EMCD) in the laminate: (a): EMCD resultant vectors in the 0-degree and 90-degree plies nrs. 31-33 and 34-36 in the upper-right quadrant of the laminate. (b): EMCD Z-component vectors in the 0-degree and 90-degree plies nrs. 31-33 and 34-36 in the upper-right quadrant of the laminate. (c) Top view of the EMCD contours in the 0-degree ply nr. 33 in all 4 quadrants of the laminate. (d): Top view of the EMCD contours in the 90-degree ply nr. 34 in all 4 quadrants of the laminate. The vector plots show the complex-real part of EMCD solution. The contour plots show the complex-magnitude part of EMCD solution.

The local current densities (EMCD) in the laminate combined with the local conductivity translate to the local Joule heating (EMJH), which is the basis for the energetic source term for the inductive heating of the laminate. Hence, the EMJH contours in the various plies are related to the EMCD contours in the same plies, Figure 5.

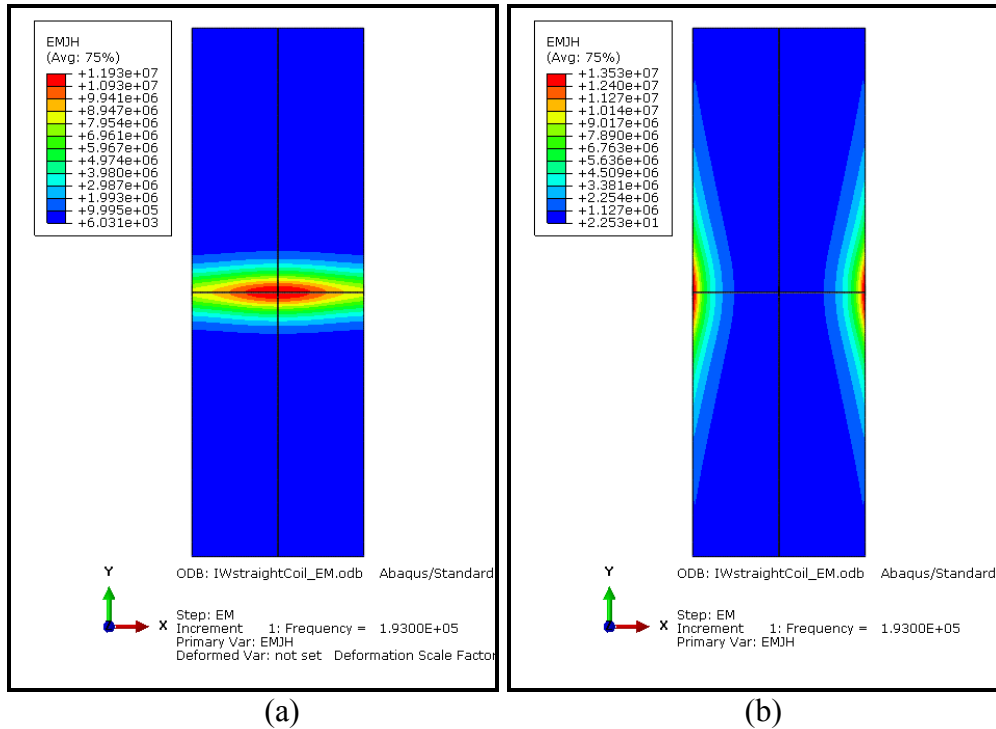


**Figure 5** Illustration of the electromagnetic Joule heating (EMJH) in the laminate: (a): Top view of the EMJH contours in the 0-degree ply nr. 33 in all 4 quadrants of the laminate. (d): Top view of the EMJH contours in the 90-degree ply nr. 34 in all 4 quadrants of the laminate.

From the electromagnetic simulation the local EMJH results can be translated to the energetic source terms in a 3D thermal simulation of the same domain. In this thermal simulation, the thermal properties of the materials and the thermal boundary conditions (e.g., radiation and convection) are prescribed. This model is then used for a heating simulation of the inductive heating experiment described above, in which a continuous heating during 37 seconds has been applied. The resulting temperatures in the top surface of the laminate then can be compared to the measured temperatures in the experiment. These measurements are made with an infrared Optris PI 640 camera, and indicate a heating pattern with maximum temperatures of about 176 °C at the left and right edges of the laminate right below the coil.

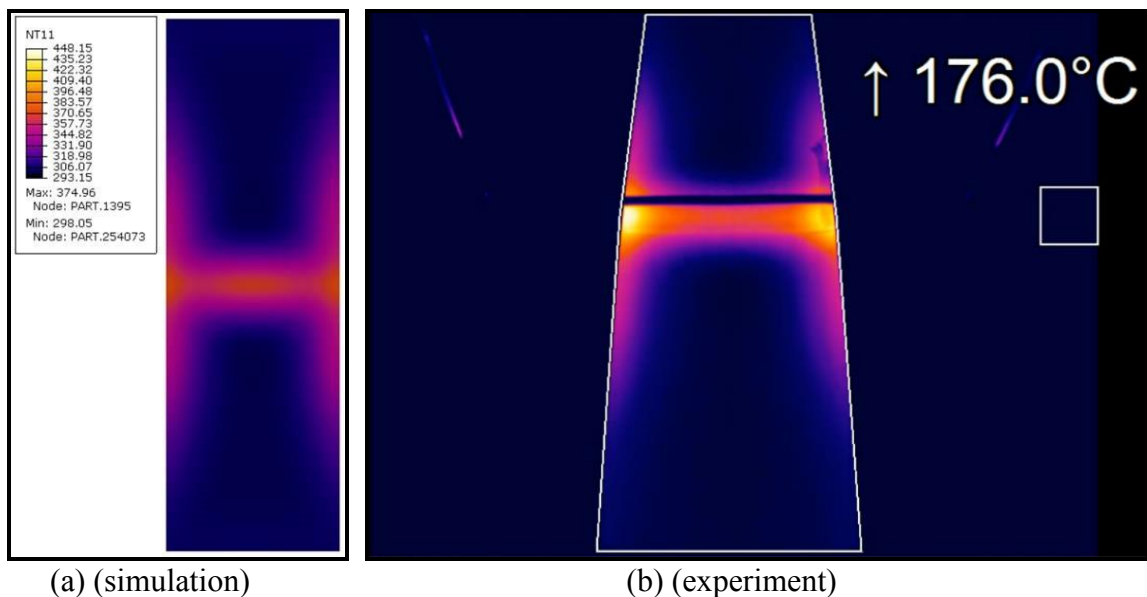




**Figure 6** Comparison of the thermal simulation results for the temperature contour with the measured temperatures in the experiment in the top surface of the laminate. (a): Simulation prediction of the temperature contour (NT11 in Kelvin; max value is around 100 °C) on the top surface of the laminate. (b): Measured temperatures in the experiment on the top surface of the laminate (purple-yellow colors; dark purple: min value: 20 °C; bright yellow: max value: 176 °C).

It is found that the temperature contours qualitatively match reasonably well, Figure 6. Especially the global predicted temperature distribution on the laminate surface is predicted reasonably accurate. However, the predicted peak temperature values appear to be too low in comparison to the experiment. This is probably due to in-accurate settings in the thermal properties of the materials and the thermal boundary conditions, which is an on-going investigation.

### 3 3D COMPONENT PLACEMENT AND ROUTING OPTIMIZATION

The introduction of more electric components on aircraft, in particular components of high power related to hybrid electric propulsion, requires careful design and installation of these electric components into their compartments or electronic- and equipment bays. One of the challenges is the detailed placement of these components in their dedicated compartments. The optimization of the volumetric space allocation of these components is a typical target, taking into account constraints on inter-component clearance or on thermal limitations. Another typical target is the optimization of inter-connectivity of cables between components aiming for minimal length and mass and accounting for certain routing constraints. Even the combination of these two, i.e. the simultaneous optimization of the components' space allocation and of the routing of their inter-connecting cables, could be considered, but will not be addressed in this paper. For simplicity we will focus here only on the sequential installation optimization problem. For illustration we will consider the installation of electric components into the electronic- and equipment bay compartment of a CS-23 turboprop aircraft. Some background of this installation problem is given in [11][5]. An illustration of the considered compartment is given in Figure 7.

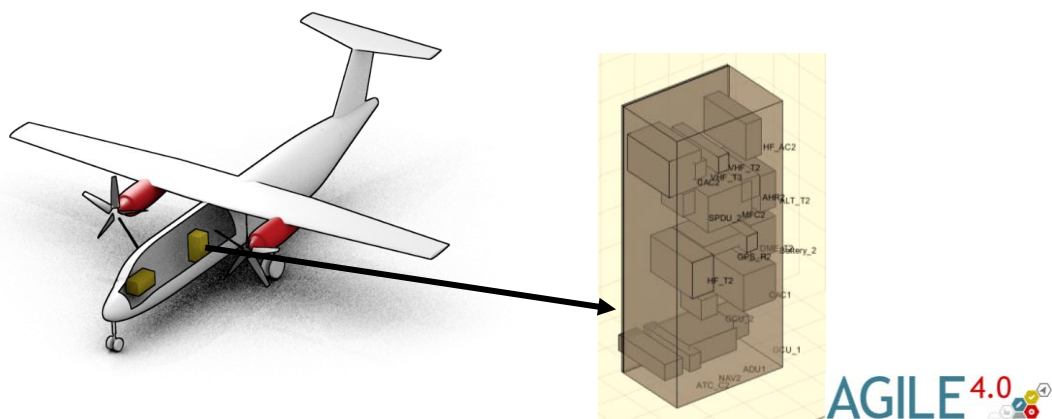


**Figure 7** Illustration of the electronic- and equipment bay compartment [11] considered in the components space allocation optimization problem [5].

To deal with the components space allocation optimization problem, simplified geometric representations of the components and the compartment are assumed. Each component and compartment are assumed as rectangular cuboids, representing the bounding box around (the main body of) their geometries. This simplification introduces some over-estimation of the

volume occupation of the components, but also some over-estimation of the available volume in the compartment. Both estimation errors may partly compensate each other, but obviously more accurate representations should be used when more detailed design of the components' installation is considered. The simplified rectangular cuboid representation of the compartment will be referred to as Space Allocation Volume (SAV). The representation of components by their bounding box, and the definition of components in the SAV are illustrated in Figure 8.

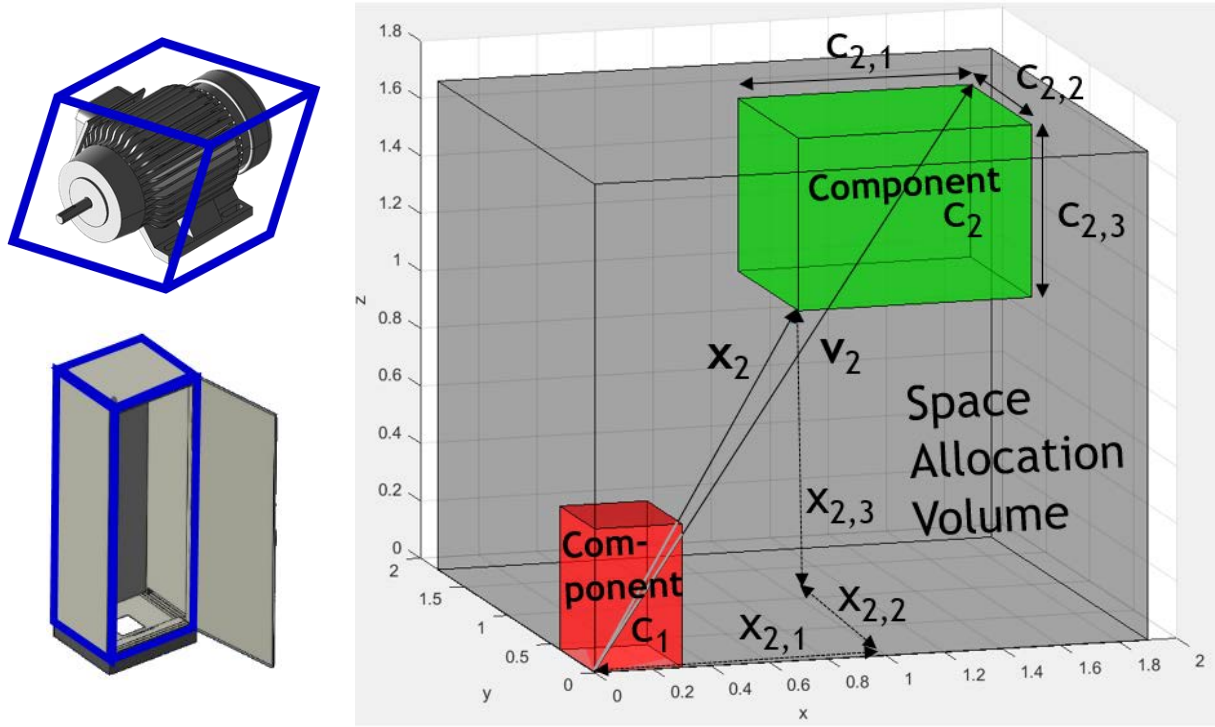


**Figure 8** Left: Illustration of the representation of components and compartments (source: grabcad.com) by their bounding boxes (indicated in blue). Right: illustration of the definition of components in the compartment (Space Allocation Volume: SAV).

For the components space allocation optimization problem formulation, we consider the following approach. An arbitrary number of  $n_c$  components are included as 3D rectangular cuboid boxes representing bounding box of any arbitrary component geometry. The box sizes are model parameters  $c_i = (c_{i,1}, c_{i,2}, c_{i,3})$ , 3 reals for each component  $c_i$ . The boxes' lower left corner locations are optimization variables  $x_i = (x_{i,1}, x_{i,2}, x_{i,3})$ , 3 reals for each component  $c_i$ . The first box is always fixed in the origin  $(0,0,0)$ , which is assumed to be in one corner of the SAV. This leads to a constrained single-objective optimization problem with  $(n_c - 1) \cdot 3$  real variables. The lower bound is 0 for all variables; upper bound is arbitrary and depends on size of the SAV, and any potential SAV clearance requirements that are taken into account. The SAV clearance would be the minimum distances between any of the components and any of the 6 faces of the SAV. Of course, this clearance can also be accounted for by re-defining the SAV as a slightly reduced bounding box of the considered compartment. Similarly, clearances between components can also be easily accounted for by using slightly extended bounding boxes for each component.

For the space allocation optimization, the considered objective is a non-linear function of the box locations  $(x_i, \forall i)$ , in this case a real scalar function of the maximum norm of the dis-

tance vectors  $\mathbf{v}_i$  of all components,  $f_{obj}=f(\|\mathbf{v}_i\|_\infty)$  where  $\mathbf{v}_i=(\mathbf{x}_i+\mathbf{c}_i)$ ,  $\forall i$ . The main constraints in the space allocation optimization problem are the no-collision constraints, which ensure that mutual geometric intrusions between any of the components is avoided. These constraints are a non-linear function of the box locations ( $\mathbf{x}_i$ ,  $\forall i$ ), yielding  $n_c*(n_c-1)/2$  real scalar inequality equations. In this space allocation optimization problem formulation, the box orientations (rotations) are not considered to limit the complexity of the optimization problem. Of course, this rather generic problem formulation can be extended with more specific additional criteria, for instance that certain components may not be placed on top of other components.

To illustrate the components space allocation optimization problem, we consider a relatively simple test problem of 8 equally sized cubic components with edge length 0.1m. These components are initially placed randomly in the cubic SAV, which has edges of 1.0m. See Figure 9, Row (1). This 3D component placement optimization problem with no-collision constraints, has 21 continuous variables (the 3D locations  $\mathbf{x}_i=(x_{i,1},x_{i,2},x_{i,3})$  of the 7 free boxes) and 28 non-linear constraints ( $n_c*(n_c-1)/2$ , where  $n_c=8$ ). This optimization problem is solved by various algorithms, like genetic algorithm (GA), pattern search (PS) and sequential quadratic programming (SQP). The solutions from the direct search solvers (GA, PS) did not deliver satisfactory solutions, i.e. insufficient minimization of the objective resulting in non-optimal packing of components around the origin. The gradient search solvers (SQP) did find satisfactory solutions, i.e. near-optimal packing of components around the origin and satisfaction of all collision constraints. But the solution required 16 iterations and 374 objective- and constraint function calls, which is mainly due to the finite-difference approximations for the gradients of objective and constraints. To improve the efficiency of the solution process, analytical expressions for the gradients of the objective- and constraint functions were derived and implemented. Then the solution requires 17 iterations and only 35 objective- and constraint function calls. Subsequently, also 0.05m clearance between all boxes was considered in the no-collision constraints, and between all boxes and SAV, for which comparable numbers of iterations and objective- and constraint function calls were needed.

We also test the components space allocation optimization on a bit larger problem: 27 equally sized cubic components with edge length 0.1m, which has 78 continuous variables for the components' 3D locations (the first box is fixed in the origin) and 351 non-linear constraints, as shown in Figure 9, Row (2). The optimization problem is solved again by the SQP algorithm, first with finite-difference approximations and subsequently with analytical expressions for the gradients of objective and constraints. With both methods we find satisfactory solutions, but of course with different computational costs: 19 iterations and 1583 objective- and constraint function calls for the finite-difference method, and 15 iterations and 34 objective- and constraint function calls for the analytical method. Again, also 0.05m clearance between all boxes was considered in the no-collision constraints, and between all boxes and SAV, for which comparable numbers of iterations and objective- and constraint function calls were needed. The results are shown in Figure 9, Row (2). For each of the optimizations, computation times are very low, less than 1 second on a standard PC, because the objective- and constraint function are based on relatively simple analytical equations.

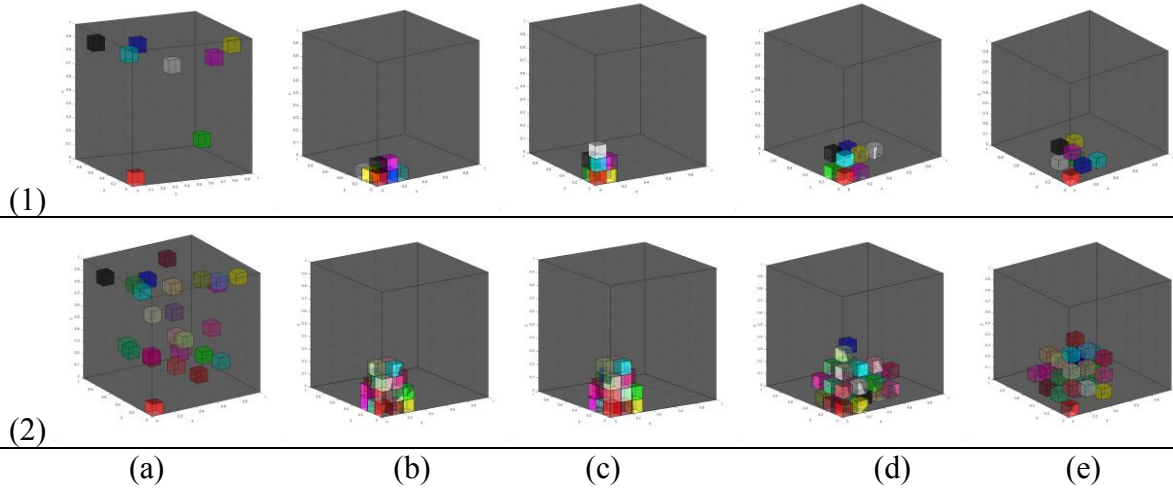


**Figure 9** Illustration of the components space allocation optimization test problems for the equally sized cubic components (colored) in a cubic SAV (grey). Row (1): 8 boxes. Row (2): 27 boxes. (a): Boxes initially placed randomly in the cubic SAV. (b): SQP optimum solution found with finite-difference approximations for the gradients of objective and constraints. (c): SQP optimum solution found with analytical expressions for the gradients of the objective and constraints. (d): SQP optimum solution including 0.05m clearance between all boxes in the no-collision constraints. (e): SQP optimum solution when including 0.05m clearance between all boxes and between all boxes and SAV.

We now return to the above-mentioned installation problem of electric components into the electronic- and equipment bay compartment of a CS-23 turboprop aircraft. In another study [11],[12] a component installation solution was determined for this problem, where the focus was on maintenance aspects (e.g. accessibility of components) and thermal risks (e.g. local overheating in the compartment) [13][14]. An optimum solution was found there, however without fully satisfying the component non-collision constraints and the constraints for placement within the compartment. Therefore, the components space allocation optimization approach with analytical gradients for the constraints that is explained above was used to resolve these constraint violations.

This optimization problem considers 18 rectangular cuboid (so non-cubic) components of various sizes, and a rectangular cuboid compartment of approximately 0.6m by 0.4m by 1.4m. The initial component installation solution for the maintenance and thermal risks aspects, but without fully satisfying the component and compartment non-collision constraints, is shown in Figure 10, row (1). This installation solution is used as initial estimate for the components space allocation optimization procedure.

In the components space allocation optimization procedure again the SQP algorithm was used, with analytical gradients for the constraints and finite difference estimation for the gradient of the objective. In the problem formulation, one small dummy component (1mm cube) was added and fixed in the origin (0,0,0) of the compartment. The objective here is based on a weighted sum of the displacement vectors of the 18 free components relative to their initial locations: this ensures that the components do not move away too far from these initial locations. The 18 components lead to 54 independent variables and 153 scalar non-collision constraints. The optimization required 42 iterations and 2439 objective- and constraint function calls. The optimized result is shown in Figure 10, row (2). In addition, also 0.015m clearance between all components was considered in the no-collision constraints, and between all com-

ponents and compartment. This optimization run required 42 iterations and 2399 objective- and constraint function calls. See Figure 10, row (3).

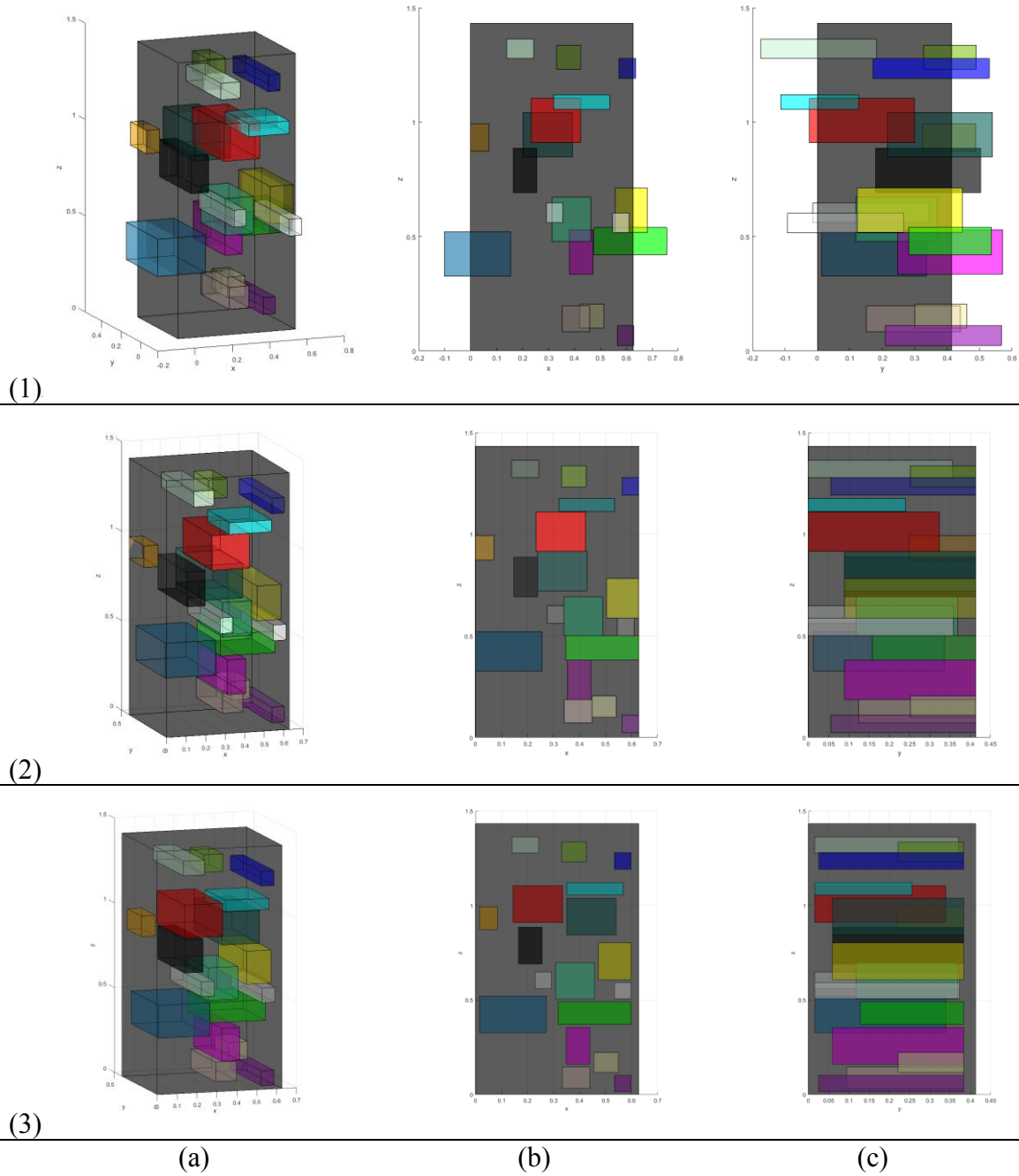


**Figure 10** Illustration of: row (1): the initial component installation solution for the maintenance and thermal risks aspects, but without fully satisfying the component and compartment non-collision constraints. Row (2): the optimized component installation solution with fully satisfied component and compartment non-collision constraints. Row (3): the optimized component installation solution with fully satisfied component and compartment non-collision constraints, and in addition accounting for 0.015m clearances between all components and between all components and compartment. Different views for each optimum solution are shown: Isometric view (a) and projections in XZ-plane (b) and YZ-plane (c), which clearly show all the non-collision constraints violations (row (1)), satisfied constraints (row (2)) and clearances (row (3)).



For the optimized component installation, we also consider the optimization of inter-connectivity of cables between the components. The drivers for such optimization are for example minimal length and mass of cables while taking into account certain routing constraints. For this optimization of inter-connectivity, we use the optimized component installation solution with fully satisfied constraints for component- and compartment non-collision, and with the 0.015m clearance between all components and between all components and compartment, as shown in Figure 10, row (3).

For the optimization of inter-connectivity of cables between the components we use NLR's software tool for component installation and routing optimization NEXT [15]. For this purpose, first the compartment SAV must be translated from its geometric definition (cuboid, in meters) to a discretized representation (triangulated STL data, in mm) for incorporation in NLR's NEXT tool, Figure 11.

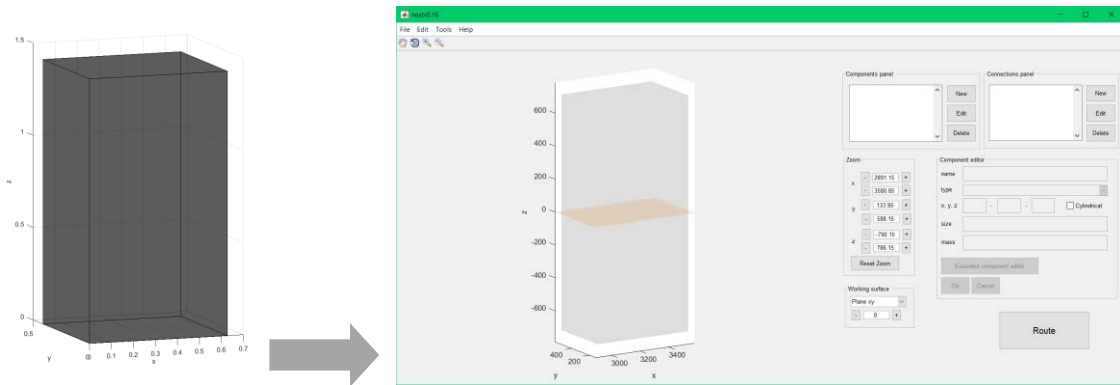


**Figure 11** Illustration of the SAV transfer process: the compartment SAV cuboid in meters (left) is translated to discretized triangulated STL data in mm for incorporation in NLR's NEXT tool [15] (right).

Subsequently, the optimized component installation is converted to a so-called system-configuration, which is defined in Microsoft Excel and can be imported into the NEXT tool. This system-configuration includes the locations, sizes and geometries of all the components, and the definitions of connectors on each of these components. The locations, sizes and geometries of components are directly and straightforward translated from the optimized component installation. The connectors represent the locations on the components where connections (for example: cables) between the components are connected. There can be any number of connectors on a component, at any location, but typically only locations on the outer surface of the component are suitable for feasible connections. To illustrate the functionality, some arbitrary example connectors are defined on the components: 1 connector at the midpoint of each face of each component. Connections can be defined between any pair of these connectors, typically from one connector on a component to another connector on another component, Figure 12. These connections at this point only represent the link between the connectors, not the exact 3D path of the cables. Various properties can be assigned to each connection, such as cable diameter and specific mass. In this example a diameter of 10mm and specific mass of 2g/mm has been used for all connections.

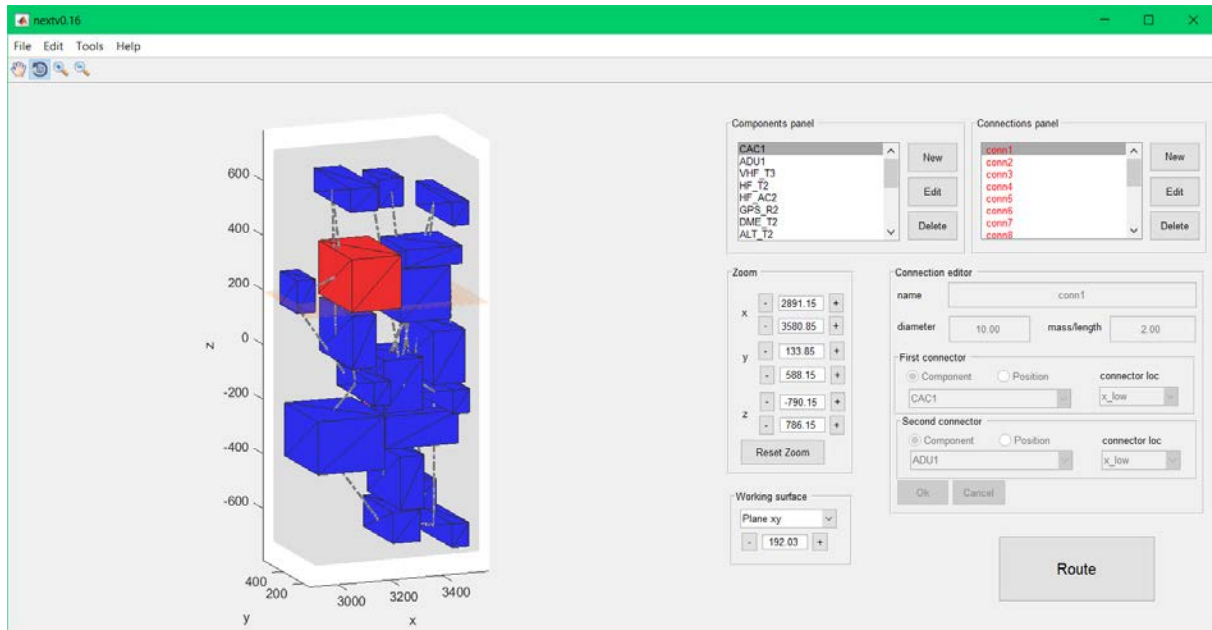


**Figure 12** Illustration of the optimized component installation that is converted to a so-called system-configuration and is imported into the NEXT tool [15]. The components are represented by the blue boxes on the left; the active box, which is selected in the components panel on the right, is highlighted in red. The connections are indicated by the grey dotted lines; the active connection, which is selected in the connection panel on the right, is highlighted in pink. In the editor panel on the right all the definitions of components, connections and connectors can be defined and changed.

The 3D paths of the cables are to be calculated by the NEXT tool from the cable routing optimization problem, Figure 13. This routing optimization problem takes into account the available space between the components in the SAV and some additional data like cable diameter clearances and possibly other criteria. Moreover, the cable routing optimization is a sequential process, so also the space occupied by previously routed cables is taken into account. This routing optimization procedure in the NEXT tool makes use of advanced graph models and is based on a modified Dijkstra's algorithm [15]. In this relatively simple example, the graph models are based on the discretized 3D SAV, which consists of approximately 400.000 cells of 10mm by 10mm by 10mm. Nevertheless, computation times for the cable routing are reasonably short, in the order of 10 seconds on a standard PC per cable for this example problem.

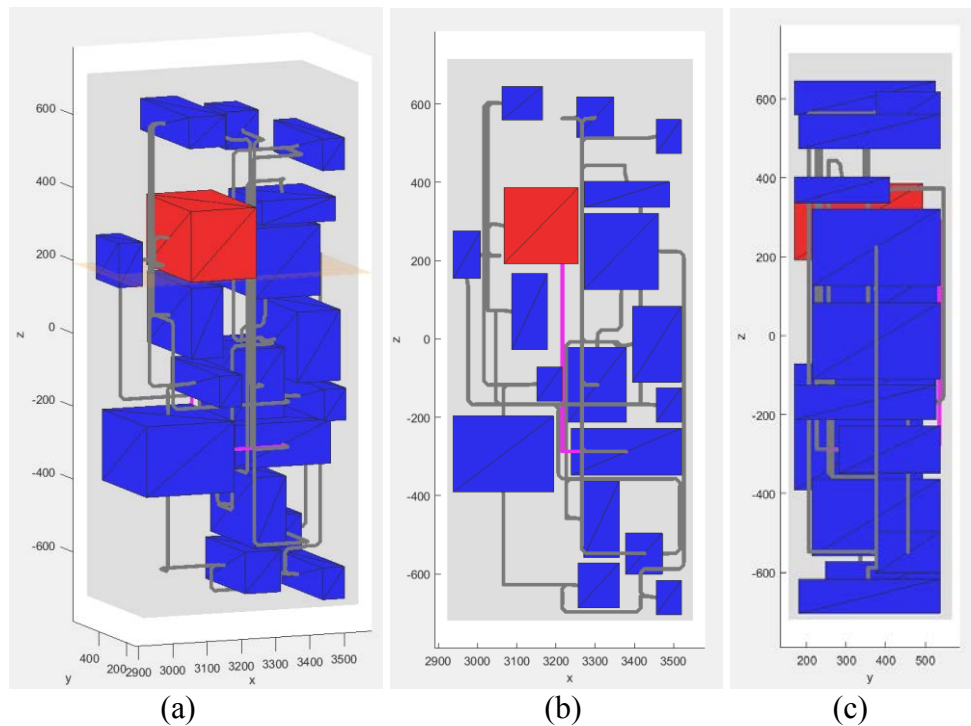


**Figure 13** Illustration of the solution of the cable routing optimization problem that is calculated with the NEXT tool for the optimized component installation. The routed cables are represented by the grey lines. The active cable, which is selected in the NEXT connection panel, is highlighted in pink. Different views of the cable routing optimization solution are shown: isometric view (a) and projections in XZ-plane (b) and YZ-plane (c), which clearly show all the cable paths between the components.

When the optimized routing for all cables has been calculated, the resulting installation solution of the optimized components and routed cables can be further checked and easily modified in the NEXT tool. For example, different connectors can be simply selected in the tool's Connection editor and the updated cable routings can be directly recalculated. When the resulting installation solution is satisfactory, it can be saved in a so-called installation file, which is a dedicated Matlab [16] .mat file containing the full definition of all components and the optimized routing for all cables. Moreover, the resulting installation can also be exported to CAD format, for example to CATIA [17]. The optimized routing for each cable is first converted to IGES representation and then included in a CATpart file. In addition, each of the components can also be converted into separate STL files. These CATpart files of the optimized routed cables and STL files of all the components can then be incorporated as a CATIA assembly in a CATProduct file, see Figure 14.

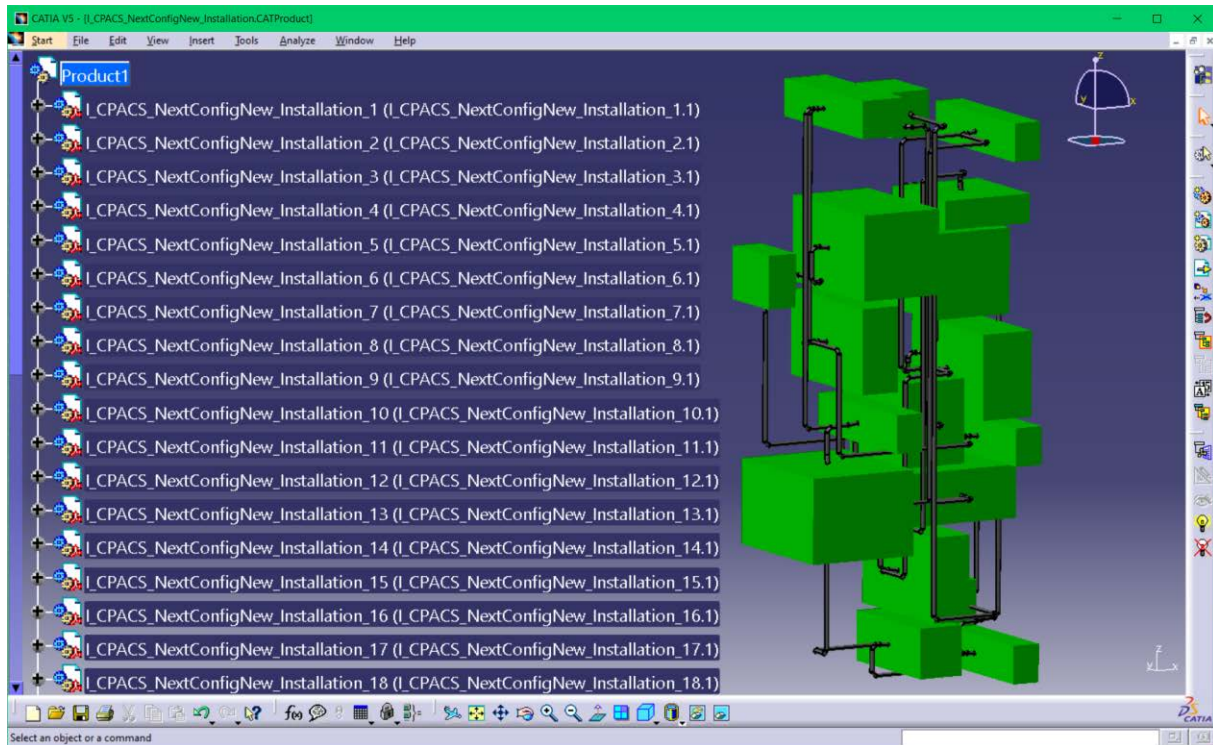


**Figure 14** Illustration of the CATIA assembly in a CATProduct file, which includes the CATpart files of the optimized routed cables and STL files of all the components.

In this way, the optimized installation can be easily transferred from the NEXT tool to CATIA, or other dedicated CAD tools, where the more detailed elaboration of the installation can be done.

#### 4 MULTI-DISCIPLINARY OPTIMIZATION OF ADVANCED FLAPS

The design and optimization of advanced flaps for large aircraft require coordinated analyses from different disciplines like aerodynamics, loads, structures, manufacturing, landing performance and cost prediction. These analyses are typically evaluated in complex sequences of dedicated software tools for the various disciplinary tasks. These tools may also be operated at specialized partners in a collaborative supply chain: analysis results are exchanged among the different partners who are responsible for the operation of their specific tool in the chain. In the AGILE4.0 project [5] such a collaborative analysis chain has been set up for the design and optimization of advanced flaps for a generic regional jet aircraft [18]. For the kinematic mechanism of the flap, two different solutions are considered: a so-called dropped hinge flap (DHF) and a so-called smart flap (SMF), see Figure 15.

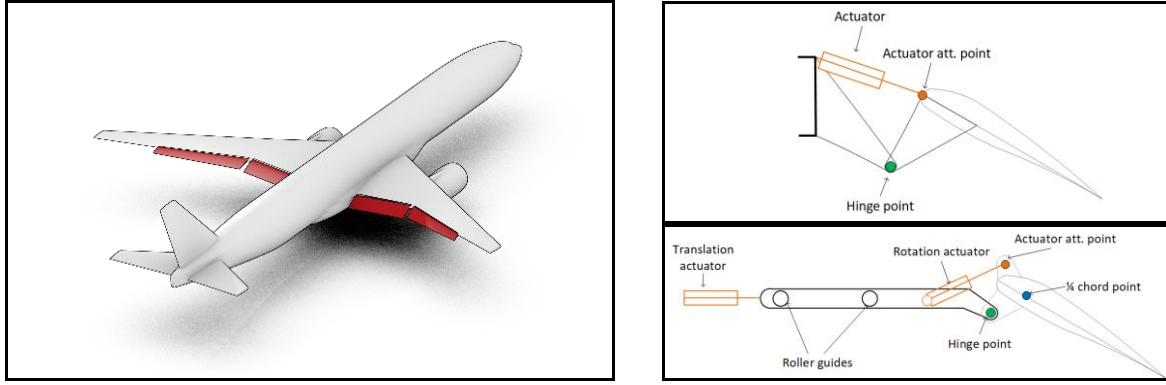


**Figure 15** Illustration of advanced flaps for a generic regional jet aircraft (left) with two different kinematic solutions (right), the dropped hinge flap (DHF) and the smart flap (SMF) [18].

The so-called extended design structure matrix (XDSM) representation of this collaborative analysis chain is shown in Figure 16, which illustrates the analyses that are considered and the exchanges between them.

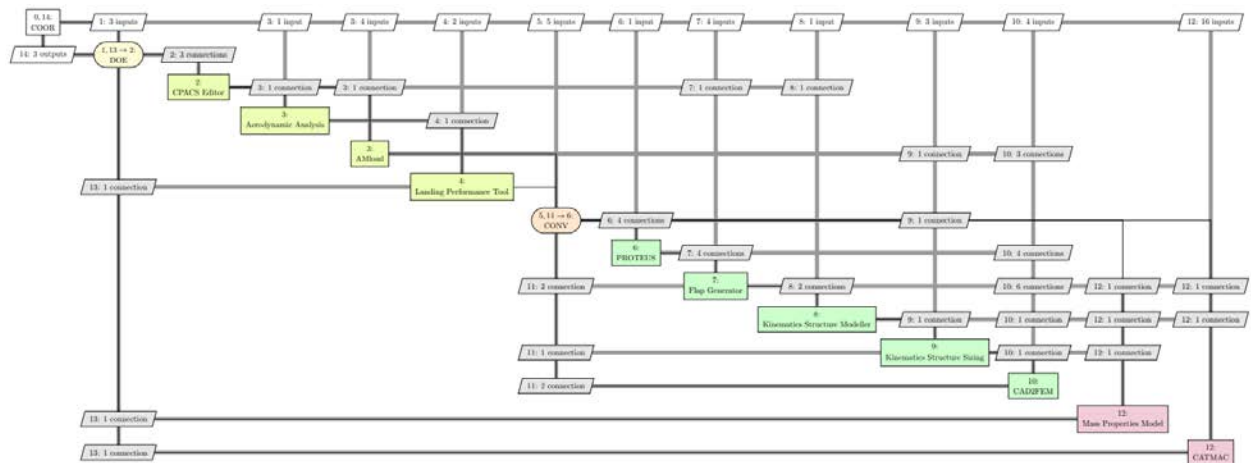


**Figure 16** Illustration of the XDSM representation of the collaborative analysis chain for the design and optimization of advanced flaps.

In the execution of this multi-disciplinary analysis chain for advanced flaps there are several complexities, for example due to the computation times and un-assured convergence of iterative solvers for the various analysis steps, and due to the intricate data exchange between the various analysis steps. Because of these complexities, the evaluation of the complete analysis chain for a single design point can be error prone and therefore difficult to automate. In automated and iterative evaluation sequences, such as in finite difference calculations and optimization iterations, these automated analysis chain evaluations are therefore hard to deploy. Instead, in this study independent analysis chain evaluations are executed to calculate coordinated series of design points in so-called design of experiments (DOE) data sets.

These DOE data sets are based on the main inputs (independent variables, or design variables) and the main outputs (dependent variables, or design criteria) of the multi-disciplinary analysis chain. These main inputs and outputs are listed and described in the Table 2.



**Table 2** The main inputs (design variables) and the main outputs (design criteria) for the DOE data sets of the multi-disciplinary analysis chain.

Design Variable	DOE bounds	Description
mechanism	DHF-SMF	Kinematic mechanism of flap, only 2 options
chord	0.15 - 0.35	Flap chord as a ratio of the local wing chord
trans	0.3 - 0.8	Flap translation as ratio of the local wing chord
pitch	150-1000	Minimal distance in mm between the ribs in the flap
Design criteria	Unit	Description
weight	[kg]	Mass of flap plus kinematic system (hinges, beams, bearings etc.)
cost	[\$]	Cost of flap plus kinematic system
land	[m]	Minimum landing distance at Maximum Landing Weight (MLW) with flaps extended in landing condition

The DOE data sets are obtained from sequential deterministic and randomized samplings: in different areas of the design domain different DOE approaches (like partial central composite designs, box-behnken designs, latin-hypercube sampling (LHS) designs) were combined into an overall DOE data set. The overall data set comprises:

- 41 points for DHF
- 36 points for SMF

For both flap mechanism types, all the 3 design variables are varied between their lower and upper bounds (chord  $\in [0.15, 0.35]$ , trans  $\in [0.3, 0.8]$ , pitch  $\in [150, 1000]$  mm). The categorical variable ‘mechanism’ is not straightforward to include directly in the optimization. Because this variable only has 2 possible values (DHF and SMF), it is more efficient to consider separate optimization problems for each of the flap mechanism types. Therefore, also separate surrogate models are created for the data sets of each of the flap mechanism types. The resulting DOE data sets for the DHF and SMF are illustrated in the Figure 17. Because of the complexities in the evaluations of the complete analysis chain, not very many successful runs were achieved and the resulting DOE data sets are rather small.

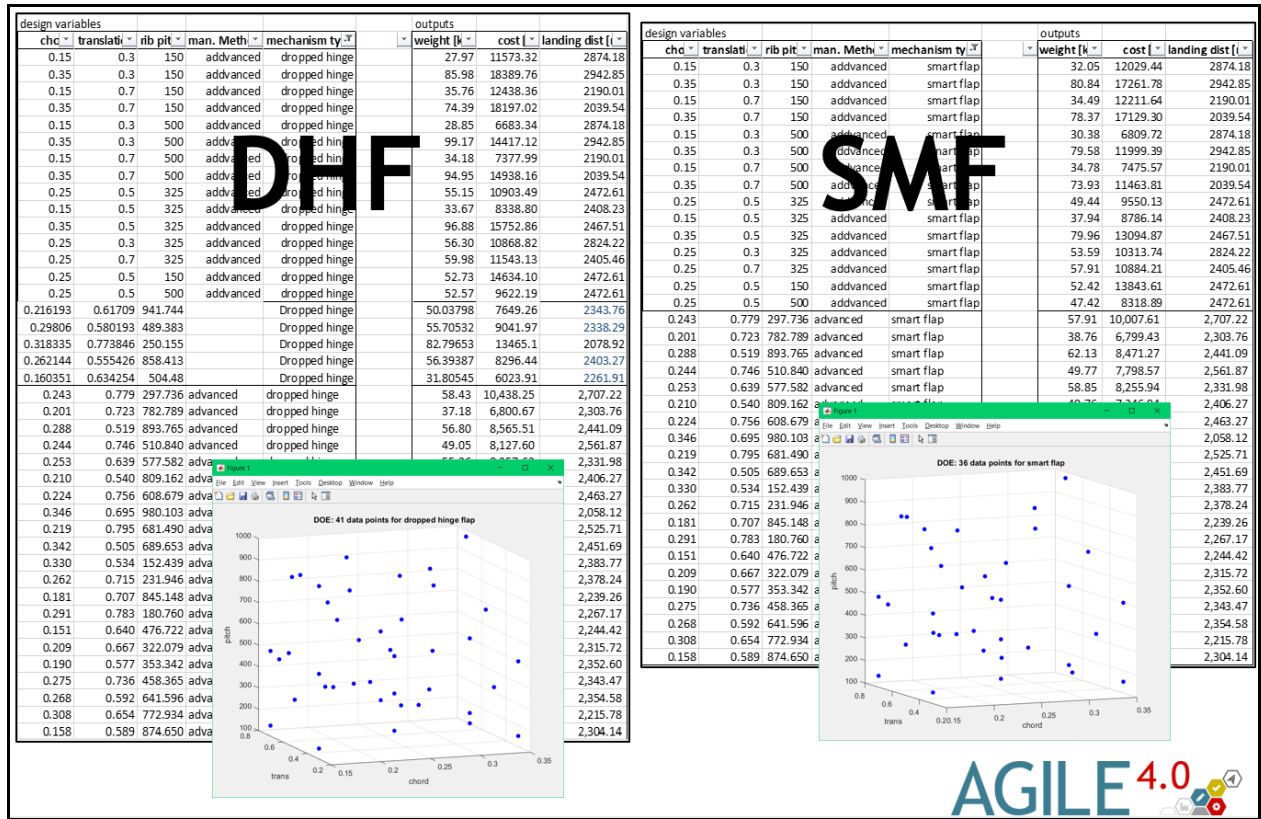


Figure 17: Illustration of the resulting DOE data sets for the DHF and SMF.

In the optimization, the 3 main design criteria are considered:

- weight: flap mass, mainly driven by structural design
- cost: flap cost, mainly driven by manufacturing
- land: a/c landing distance, mainly driven by flap aero-performance

For each of these 3 main design criteria separate surrogate models are created. Because of the rather small DOE data sets, the selection of the most appropriate surrogate model shall be made quite carefully. Therefore, various methods are tested and evaluated for these surrogate models, among others:

- Scattered-interpolant (SCI)
- Radial-basis functions (RBF)
- Generalized-regression nets (GRN)
- Feed-forward neural nets (FFN)
- Gaussian-process regression (GPR) (kriging)

For the DHF data set, the GPR surrogate models achieve the best accuracy: the mean and max values of the absolute percentage errors of predictions on the DOE data set are as follows:

- weight: [mean, max]: [7.8%, 19.7%]
- cost: [mean, max]: [5.4%, 17.2%]
- land: [mean, max]: [0.4%, 1.7%]

To assess the accuracy of the surrogate models in the whole design domain, the error values in the DOE data sets are interpolated in the whole domain. For the DHF, the percentage errors estimations on a 4000 point random LHS dataset in the whole design domain are as follows (see Figure 18):

- weight: percentage error  $\in [-49\%, +45\%]$
- cost: percentage error  $\in [-14\%, +30\%]$

- landing: percentage error  $\in [-1\%, +8\%]$

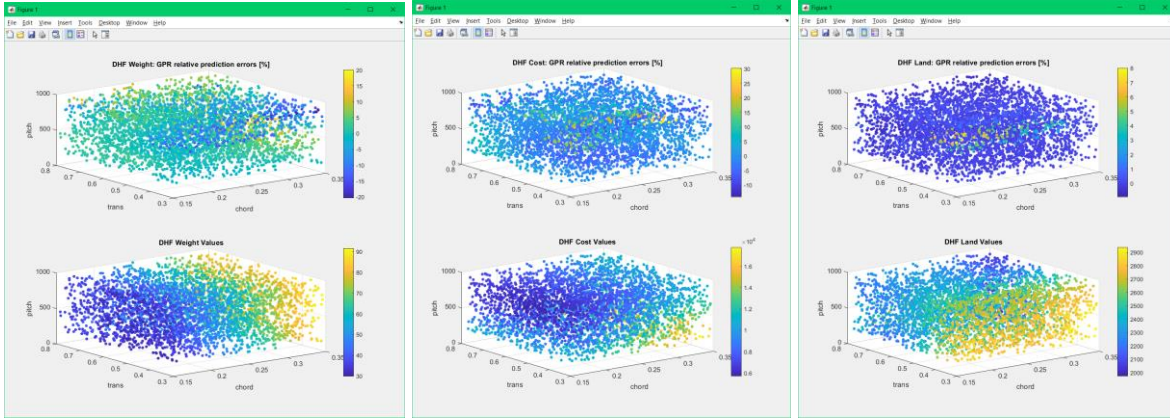


**Figure 18: Illustration of the percentage errors estimations on a 4000 point LHS dataset in the whole design domain for the DHF.**

For the SMF also the GPR surrogate models achieve the best accuracy: the mean and max values of the absolute percentage errors of predictions on the DOE data set are as follows:

- weight: [mean, max]: [7.8%, 19.7%]
- cost: [mean, max]: [5.4%, 17.2%]
- landing: [mean, max]: [0.4%, 1.7%]

For the SMF, the percentage errors estimations on 4000 point LHS dataset in design domain are as follows (see Figure 19):

- weight: percentage error  $\in [-35\%, +38\%]$
- cost: percentage error  $\in [-26\%, +21\%]$
- landing: percentage error  $\in [-1\%, +12\%]$

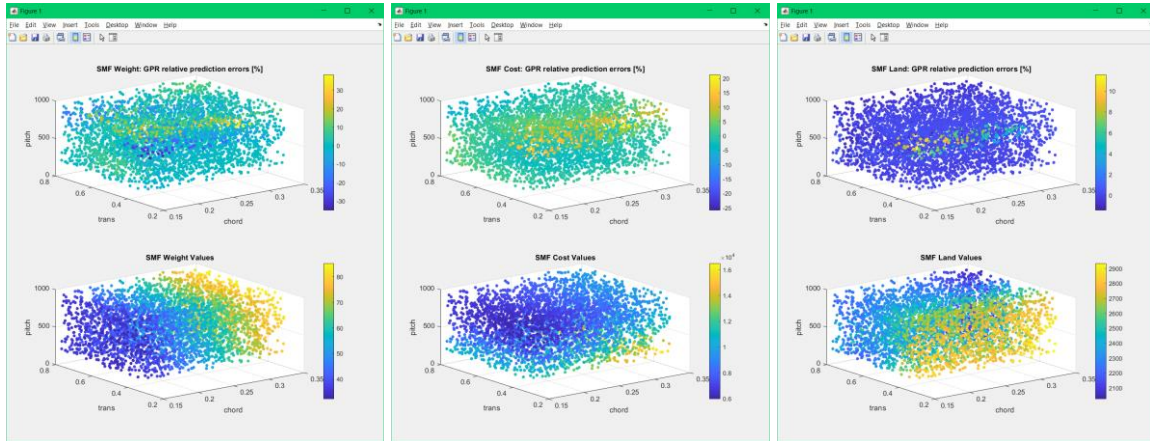


**Figure 19: Illustration of the percentage errors estimations on a 4000pt LHS dataset in the whole design domain for the SMF.**

With the selected methods, the surrogate models' evaluations are very fast. Typically for multi-objective optimizations in the order of  $1e5$  function evaluations are required. With the selected methods these  $1e5$  evaluations can be run in just few seconds on a standard PC.

Several optimization evaluations have been performed with the surrogate models for the DHF and SMF design criteria. First some Pareto ranking evaluations were done on random search data sets in the design domain, in order to determine the regions of interest.

Subsequently several multi-objective optimizations (MOO) using NSGA2 (non-dominated sorting genetic algorithm) search were performed for more detailed, coordinated and better targeted search. In these MOO evaluations, the minimum weight and cost are used as objectives, and the landing field length of less than 2500m is used as non-linear constraint function.

First for the DHF, this MOO evaluation (NSGA2 weight-cost Pareto front for land<2500) is done in the large design space with lower- and upper bounds:

- lb = [0.15,0.3,150]
- ub = [0.35,0.8,1000]

The population size is 1000 and the number of generations needed for convergence of the Pareto front is 125, with a total number of objectives and constraint function evaluations of 125001. The resulting Pareto front has 350 points, indicated by the green dots in the plots in Figure 20.

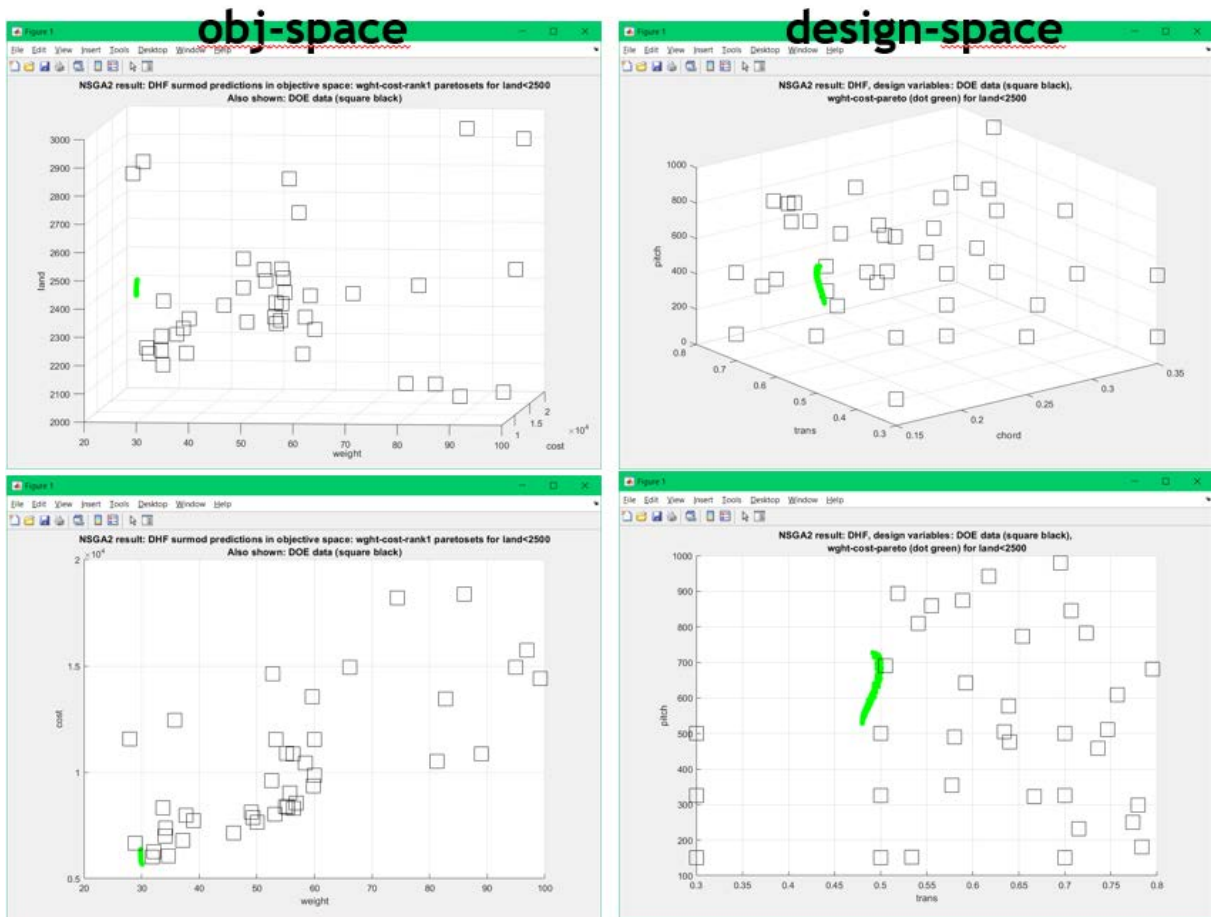


**Figure 20: Illustration for the DHF of the Pareto front (green dots) and the original DOE design points (black squares) in the 3D weight-cost-landing-objective space (left) and the 3D chord-trans-pitch-design space (right).**

Similarly, for the SMF an analogous MOO evaluation was performed, yielding a slightly different Pareto front. The population size is also 1000 and the number of generations needed for convergence of the Pareto front is 132, with a total number of objectives and constraint

function evaluations of 132001. The resulting Pareto front has 350 points, indicated by the green dots in the plots in Figure 21.

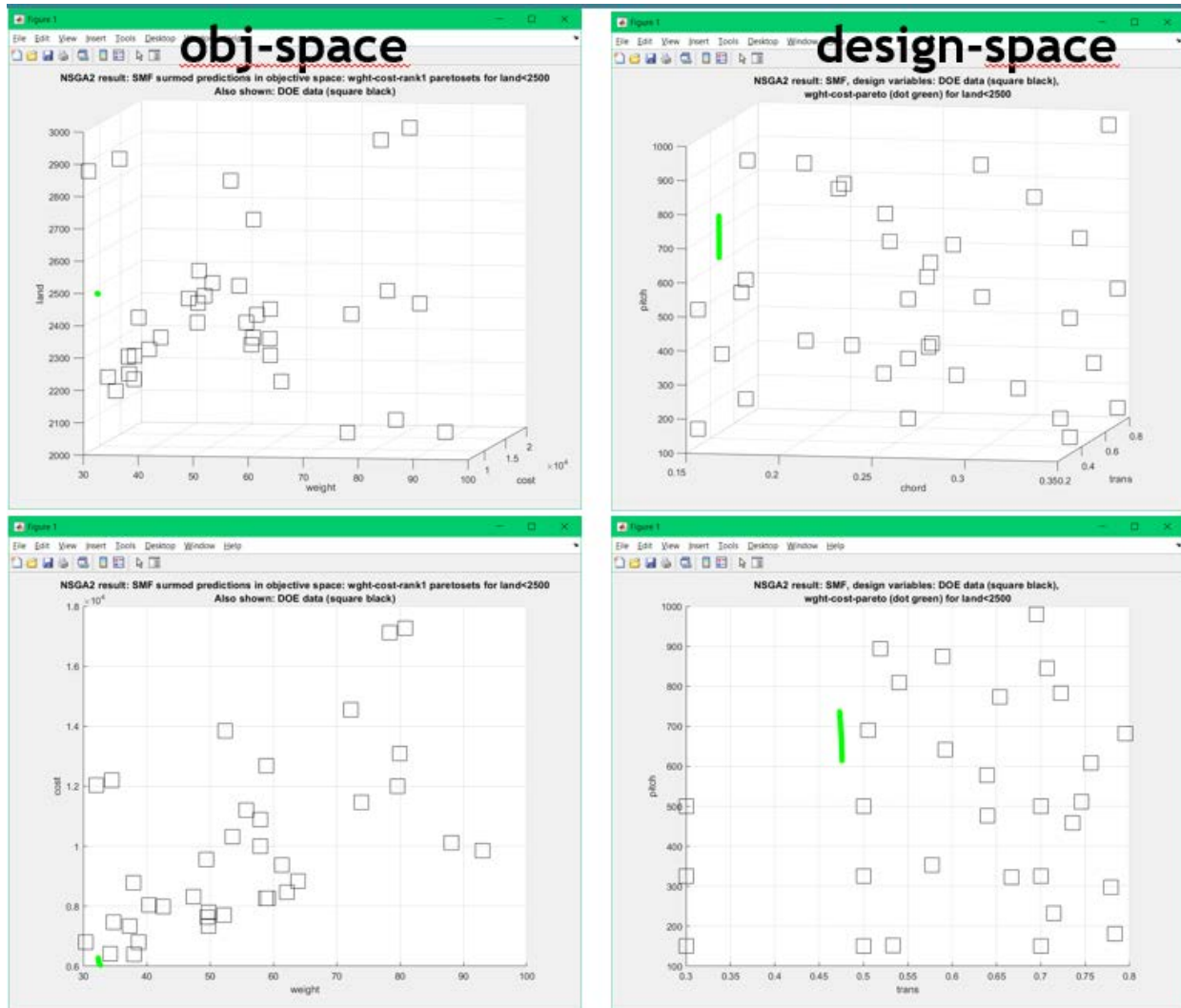
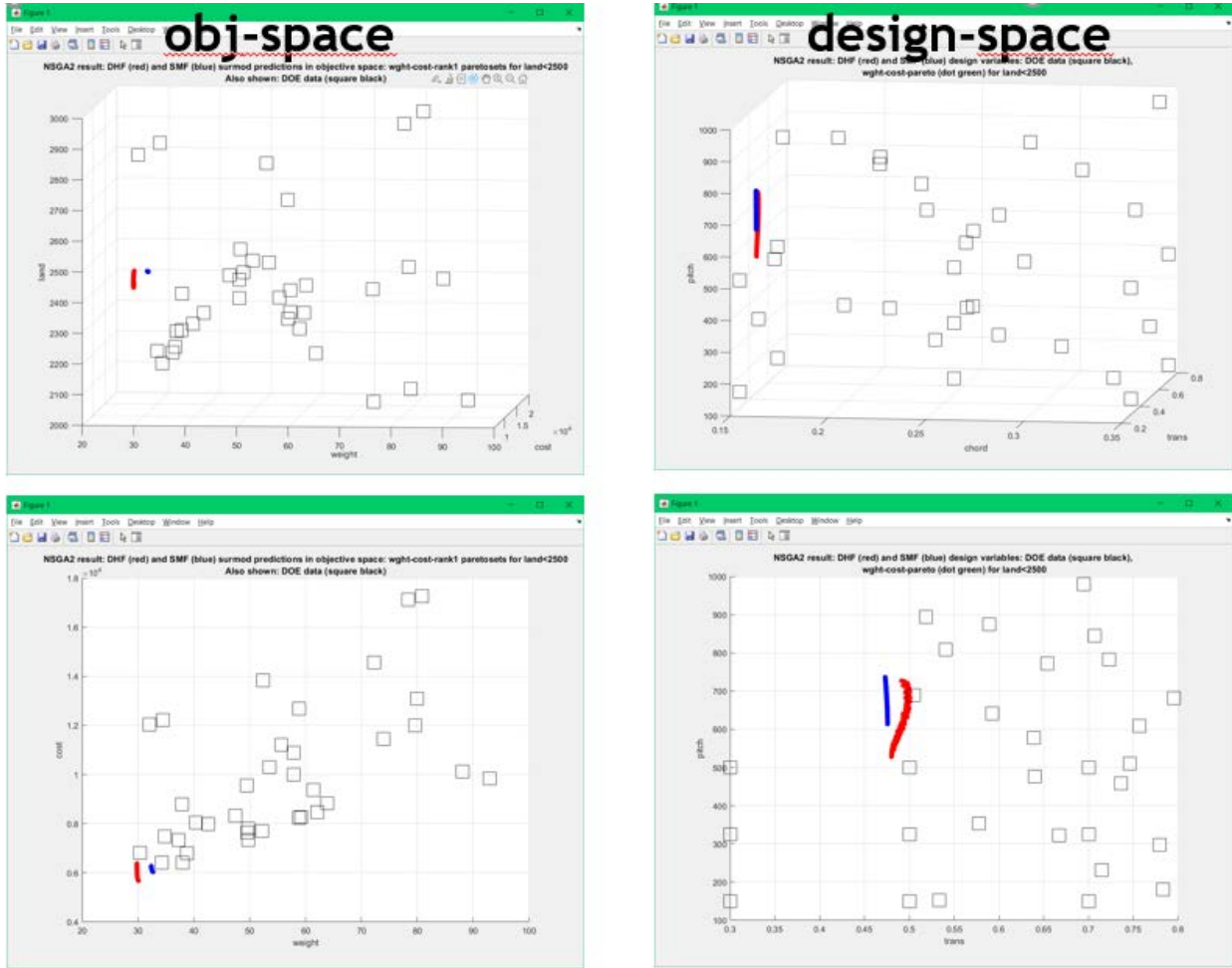


Figure 21: Illustration for the SMF of the Pareto front (green dots) and the original DOE design points (black squares) in the 3D weight-cost-landing-objective space (left) and the 3D chord-trans-pitch-design space (right).

To determine the overall optimum design, we compare the Pareto fronts of the DHF and the SMF (Figure 22).





**Figure 22: Illustration for the Pareto front data points for the DHF (red dots) and for the SMF (blue dots). Plots are given for the 3D weight-cost-landing-objective space (left) and the 3D chord-trans-pitch-design space (right).**

The DHF results clearly dominate the SMF results: the DHF Pareto points have lower values for both weight and cost than the SMF Pareto points. In design space, the Pareto points for both flap mechanism types are close together, all close to the lower bound for the chord (0.15) and trans values of about 0.48 and pitch of around 650mm.

This study demonstrates the potential of surrogate based optimization approaches for complex multi-disciplinary collaborative design and analysis processes. In this way, the complexities in the execution of such multi-disciplinary analysis chains can be de-coupled from the automated and iterative evaluation sequences in the optimization calculations. The computational efficiency of the surrogate models allows for very quick optimization evaluations involving huge numbers of function evaluations. Of course, the limited accuracy of the surrogate models requires careful checking of the optimization results by re-evaluation of the optimum design points with the multi-disciplinary analysis chain. This latter aspect has not been demonstrated in this study, but has been considered in proceeding investigations in the AGILE4.0 project [5].

## 5 CONCLUSIONS

Advanced modelling, simulation and optimization methodologies are indispensable for successful application of innovative technologies and radical innovations in modern aviation. Some example applications have been presented where the development of innovative technologies is supported by increasingly digitalized methods, tools and technologies. In particular, advanced FEM modelling and EM analysis have been shown for application to induction welding of TP-CFRP structures. Also, some fundamental methods and tools for computational geometry and graph based modelling have been demonstrated for application to automated placement and routing of electric components in confined compartments on-board hybrid/electric aircraft. And some advanced methodologies have been presented for surrogate-based optimization of complex multi-disciplinary design and analysis processes for advanced flaps. These methodologies and their example applications and some of their potential implications on innovative aeronautic technologies have been indicated. Further work is needed to enhance these methodologies and their adoption in standard aeronautic development processes.

## ACKNOWLEDGEMENTS

STUNNING project: This project has received funding from the Clean Sky 2 Joint Undertaking (JU) under grant agreement No 945583. The JU receives support from the European Union's Horizon 2020 research and innovation programme and the Clean Sky 2 JU members other than the Union.

AGILE 4.0 project: This research has received funding from the European Union Horizon 2020 Programme under grant agreement n° 815122.

The inputs for the second and third example applications from the AGILE 4.0 colleagues Philipp Hansmann from RWTH, Jente Sonneveld from TUD and Ton van der Laan from GKN, are gratefully acknowledged.

## DISCLAIMER

STUNNING project: The results, opinions, conclusions, etc. presented in this work are those of the author(s) only and do not necessarily represent the position of the JU; the JU is not responsible for any use made of the information contained herein.

## REFERENCES

- [1] Clean Aviation Joint Undertaking, The next generation Multifunctional Fuselage Demonstrator — leveraging thermoplastics for cleaner skies. [https://www.clean-aviation.eu/sites/default/files/2021-10/CLEAN\\_SKY\\_Article\\_MultiFuse.pdf](https://www.clean-aviation.eu/sites/default/files/2021-10/CLEAN_SKY_Article_MultiFuse.pdf), 2021.
- [2] Y. Xie, A. Savvarisal, A. Tsourdos, D. Zhang, J. Gu, Review of hybrid electric powered aircraft, its conceptual design and energy management methodologies. Chinese Journal of Aeronautics, Volume 34, Issue 4, pp. 432-450, ISSN 1000-9361, 2021. <https://doi.org/10.1016/j.cja.2020.07.017>.

- [3] M. Fioriti, P. Della Vecchia, G. Donelli, P. Hansmann, Assessing the Integration of Electrified On-Board Systems in an MDAO framework for a small transport aircraft. Proc. AIAA Aviation, August 2021. <https://doi.org/10.2514/6.2021-3094>.
- [4] T. van der Laan, A-L. Bruggeman, B. Van Manen, Z. Wang, D. Peeters, J. Sonneveld, H. Timmermans, Bringing Manufacturing into the MDO domain using MBSE. Proc. AIAA Aviation, Chicago, June 2022. <https://arc.aiaa.org/doi/10.2514/6.2022-3721>.
- [5] AGILE 4.0 project, <https://www.agile4.eu/>.
- [6] A. Yousefpour, M. Hojjati, and J.-P. Immarigeon, Fusion Bonding/Welding of Thermoplastic Composites, Journal of thermoplastic composite materials, 17:303, 2004.
- [7] T.J. Ahmed, D. Stavrov, H.E.N. Bersee, and A. Beukers, Induction welding of thermoplastic composites - an overview, Composites Part A: applied science and manufacturing, pp. 1638—1651, 2006.
- [8] Simulia, <https://www.3ds.com/products-services/simulia/products/abaqus/>.
- [9] A.J. de Wit, N. van Hoorn, L. Straathof, W.J. Vankan, Numerical simulation of inductive heating in uni-directional thermoplastic uni-directional cross-ply laminates composites, Frontiers in Materials, section Polymeric and Composite Materials, Submitted on: 31 Jan 2023.
- [10] Toray Advanced Composites, <https://www.toraytac.com/>.
- [11] P. Hansmann, J. Ortmann, E. Stumpf, A Maintainability Prediction and Optimization Framework for Multi Component Systems in the Preliminary Aircraft Design Stage, Deutscher Luft- und Raumfahrtkongress 2023, Stuttgart, 2023.
- [12] J. Ortmann, A Methodology for the Quantitative Assessment of the Aircraft Systems Accessibility, MSc thesis RWTH Aachen University, 2021. <https://doi.org/10.5281/zenodo.5776823>.
- [13] F. Sanchez, S. Liscouët-Hanke, Thermal risk prediction methodology for conceptual design of aircraft equipment bays, Aerosp. Sci. Technol., 104 (2020), Article 105946, <https://doi.org/10.1016/j.ast.2020.105946>.
- [14] F. Sanchez, A.M. Huzaiifa, S. Liscouët-Hanke, Ventilation considerations for an enhanced thermal risk prediction in aircraft conceptual design, Aerospace Science and Technology, Volume 108, 2021, 106401, ISSN 1270-9638, <https://doi.org/10.1016/j.ast.2020.106401>.
- [15] W.J. Vankan, R. Maas, S.M. Moghadasi, Optimization tool for equipment placement and routing in more electric aircraft, Proc. Aerospace Europe Conference - AEC2020, February 25-28, 2020, Bordeaux, France. NLR-TP-2020-011.
- [16] Mathworks, <https://nl.mathworks.com/products/matlab.html>.
- [17] Dassault Systemes, <https://www.3ds.com/products-services/catia/>.
- [18] T. van der Laan, A-L. Bruggeman, B. Van Manen, Z. Wang, D. Peeters, J. Sonneveld, H. Timmermans, Bringing Manufacturing into the MDO domain using MBSE, AIAA Aviation, Chicago USA, June 2022. <https://arc.aiaa.org/doi/10.2514/6.2022-3721>.